The azimuthal distribution of ejecta mass from oblique impacts into sand

Alice C. Quillen[a,*], Sean Doran[a]

[a]*Department of Physics and Astronomy, University of Rochester, Rochester, NY 14627, USA*

Abstract

We measure ejecta mass as a function of azimuthal and impact angle for 104 m/s oblique impacts into sand. We find that the ejecta mass distribution is strongly sensitive to azimuthal angle with up to 8 times more mass in ejecta on the downrange side compared to the uprange side. Crater radii, measured from the site of impact, are measured at different impact and azimuthal angles. Crater ejecta scaling laws are modified to depend on azimuthal and impact angle. We find that crater radii are sensitive to both impact and azimuthal angle but the ejecta mass as a function of both angles can be estimated from the cube of the crater radius without an additional angular dependent function. The ejecta distributions are relevant for processes that depend upon the integrated properties of intermediate velocity impacts occurring in the outer solar system and possibly during planetesimal formation.

1. Introduction

Because ejecta from an impact can escape an asteroid or planetesimal, the velocity and mass distributions of ejecta affect the total momentum imparted to the asteroid and as a consequence, its deflected trajectory (Jutzi and Michel, 2014; Cheng et al., 2016; Thomas et al., 2023). The ratio of the change in center of mass momentum and the projectile momentum is known as the momentum transfer efficiency parameter, and is relevant for mitigation strategies for deflection of potentially hazardous asteroids (Holsapple and Housen, 2012). Over a long period of time, impacts cumulatively exert a torque on a spinning body, which can reduce its rotation rate (Dobrovolskis and Burns, 1984). The distribution of ejecta in a lower velocity impact regime (10 to 50 m/s) is relevant for estimating collision evolution of asteroids (Farinella et al., 1992; Campo Bagatin et al., 1994), accretion, erosion and particle transport on young and forming planetesimals (Quillen et al., 2024).

While most craters on asteroid and satellite surfaces, including the Moon, are nearly round, impacts on astronomical bodies rarely have projectile velocity vector nearly normal to the surface. We take the impact angle θ_I to be the angle between the plane tangent to the surface at the point of impact and the projectile momentum vector, as seen in a reference frame in which the surface is stationary. With this convention, grazing impacts have low impact angle. More than 50% of impacts are expected to occur at impact angles between 30 and 60° (Melosh and Pierazzo, 2000). Normal impacts on a homogeneous and isotropic level substrate exhibit rotational symmetry about an axis normal to the surface that intersects the site of impact. Azimuthal symmetry facilitates integrating over the ejecta mass and velocity distributions, consequently scaling laws based on dimensionless parameters for estimating crater size and ejecta mass and velocity distributions predominantly apply to normal impacts (Holsapple, 1993; Housen and Holsapple, 2011; Scheeres et al., 2010; Çelic et al., 2022).

The momentum transfer caused by an impact can be computed from the integral of the fraction of ejecta distribution that escapes the planetesimal (e.g., Dobrovolskis and Burns 1984; Farinella et al. 1992; Raducan et al. 2022). An estimate for the torque caused by impacts on asteroids requires taking into account the distribution of impact angles in the population of projectiles (Dobrovolskis and Burns, 1984). This motivates us to improve upon estimates for the ejecta distributions of oblique impacts. The low or intermediate velocity regime (about 20 to 100 m/s) would be relevant for impacts from particles in the protosolar nebula (Quillen et al., 2024) and for impacts in the outer solar system (Greenstreet et al., 2019).

Impact craters formed at normal impact angle obey scaling relationships for crater size and volume (Holsapple, 1993; Housen and Holsapple, 2011; Scheeres et al., 2010; Çelic et al., 2022; Mazur et al., 2022) based on the dimensionless parameters

$$\pi_2 = \frac{g_a a_{pj}}{u_{pj}^2} \tag{1}$$

$$\pi_3 = \frac{Y_a}{\rho_a u_{pj}^2} \tag{2}$$

$$\pi_4 = \frac{\rho_a}{\rho_{pj}}. \tag{3}$$

Here g_a is the gravitational acceleration at the site of impact, ρ_a is the density of the substrate, Y_a is substrate

strength, u_{pj} is projectile velocity, ρ_{pj} is projectile density, and a_{pj} is the projectile radius. Recent compilations of crater dimensions suggest that these scaling laws are remarkably good at matching crater properties, such as radius and volume, over a wide range of impact and substrate properties, and including a low velocity regime (Holsapple, 1993; Housen and Holsapple, 2011; Housen et al., 2018; Çelic et al., 2022; Mazur et al., 2022). Assuming that a projectile acts like a point source when considering crater-related phenomena, Housen and Holsapple (2011) developed power-law scaling relations for the properties of ejecta curtains, with ejecta properties such as ejecta speed and ejected mass dependent on the horizontal distance from the site of impact.

Ejecta mass and velocity distribution functions for oblique impacts, when integrated, are directly related to the momentum transfer efficiency and the change in spin caused by an impact. The ejecta distributions derived in the point source approximation by Housen and Holsapple (2011) were modified to depend upon azimuthal angle and ejecta angle and then fit to velocity and mass ejecta distributions measured from shock physics code simulations (Raducan et al., 2022). Dobrovolskis and Burns (1984) used a power-law form for the ejecta distributions, based on impact experiments by Stoeffler et al. (1975), to estimate a cumulative torque on asteroids due to impacts. Improved measurements of ejecta distributions for oblique impact would help improve estimates for momentum transfer and torque caused by impacts.

Ejecta from high velocity oblique impacts have been tracked using high speed cameras (Anderson et al., 2003, 2004; Anderson and Schultz, 2006) giving measurements of both ejecta angle and velocity distributions as a function both impact angle θ_I and azimuthal angle ζ measured in the substrate plane. Azimuthal variations in ejecta angle and velocity imply that there is asymmetry in the subsurface response (Anderson et al., 2003, 2004; Anderson and Schultz, 2006) and this was verified for oblique impacts into sand using embedded accelerometers (Suo et al., 2024). Simulations of high velocity impacts have been used to measure the sensitivity of ejecta velocity, angle and mass distributions to both impact and azimuthal angle (Raducan et al., 2022).

Ejecta particle velocity can be tracked in videos taken with high speed cameras (Anderson et al., 2003, 2004; Anderson and Schultz, 2006; Tsujido et al., 2015), but because particles in an ejecta curtain can obscure material behind them, it is more challenging to measure the ejecta mass distribution from videos. Trays laid on the surface or mounted above the surface can be used to capture ejecta which later are weighed, giving constraints on the mass distribution of the ejecta curtain (Stoeffler et al., 1975; Wünnemann et al., 2016; Luther et al., 2018; Mazur et al., 2022). We build upon our prior experimental study of intermediate velocity oblique impacts (Suo et al., 2024) by similarly using trays to catch ejecta at different azimuthal angles. Crater depth profiles at different impact angles

are used to model the azimuthal and impact angular dependence of crater radius. We extend ejecta crater scaling models for normal impacts to describe the azimuthal and impact angle dependence of the ejecta mass distribution. Our distributions may be used in models that integrate over ejecta properties to estimate momentum transfer and torque from intermediate velocity oblique impacts.

2. Experiments

Our experiments build upon those described by Suo et al. (2024), with projectile and substrate properties summarized in Table 1. Illustrations of our experiments are shown in Figure 1. Small plastic spherical projectiles (referred to as pellets or BBs) are launched with an airsoft gun at a speed of $v_{imp} = 103$ to 105 m/s. The substrate is fine sand with grain semi-major axis mean value $a_s \approx 0.3$ mm, as described in previous experiments (Wright et al., 2020). Dimensionless constants π_2, π_3, π_4, used to characterize crater scaling regimes are also listed in Table 1 along with their definitions (following Holsapple 1993; Housen and Holsapple 2011; Housen et al. 2018). Experimental measurements suggest that rocky granular or regolith systems would have an effective strength of order $Y_a \approx 500$ Pa (Brisset et al., 2022) and we adopt that value to compute the dimensionless parameter π_3.

Table 1: Properties of the Projectiles and substrate and dimensionless numbers

Quantity	Symbol	Value
Projectile Mass	m_{pj}	0.20 ± 0.002 g
Projectile Radius	a_{pj}	2.98 ± 0.005 mm
Projectile Density	ρ_{pj}	1.80 g cm^{-3}
Projectile Speed	u_{pj}	104 ± 1 m/s
Substrate density	ρ_a	1.5 g cm^{-3}
Washtub rim radius	R_{tub}	25.1 cm
Washtub depth	H_{tub}	25 cm
Crater radius	$R_{cr,n}$	2.85 cm
Crater volume	$V_{cr,n}$	14.7 cm^{-3}
Dimensionless params.	Formula	Value
π_2	$g_a a_{pj}/u_{pj}^2$	2.7×10^{-6}
π_3	$Y_a/(\rho_a u_{pj}^2)$	3×10^{-5}
π_4	ρ_a/ρ_{pj}	0.83
π_R	$R_{cr,n}(\rho_a/m_{pj})^{\frac{1}{3}}$	5.6
π_V	$V_{cr,n}\rho_a/m_{pj}$	110

The parameter π_3 is computed with Y_a=500 Pa.

Following Housen and Holsapple (2011), a substrate particle is considered ejected as it crosses the plane that was the surface of the substrate prior to impact, as shown in Figure 1a. In this plane, the distance from impact is x and v_{ej} is the ejection velocity. After the transient crater has formed, we take crater radius R_{cr} to be the radius from the site of impact where the crater surface crosses the level of the surface prior to impact, and as shown in Figure 1a. The radius R_{rim} is the distance from impact site to
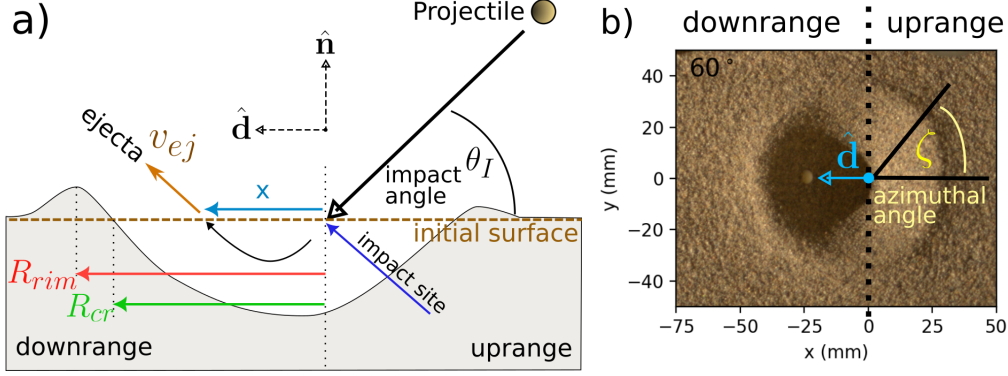
Figure 1: a) We show a side view illustration of a transient crater created by an oblique impact at impact angle θ_I. Distances are measured in the plane of the level surface prior to impact. The crater radius R_{cr} is the distance between impact site and where the crater surface crosses the level of the surface prior to impact (following Housen and Holsapple 2011). The crater rim radius R_{rim} is the distance in the surface level plane between impact point and rim peak. The ejecta launch point is given in terms of x which is a distance from the site of impact. We also illustrate normal and down range directions $\hat{\mathbf{n}}$ and $\hat{\mathbf{d}}$. The tan shading shows the transient crater. The brown dashed line shows the level of the surface prior to impact. b) A view from above illustrating the downrange direction and the azimuthal angle ζ which is measured with origin the site of impact. With projectile originating from the right, downrange is to the left. The background is a photograph of a laboratory transient crater with an impact angle of $\theta_I = 60°$. After impact, the BB projectile remained in the crater and can be seen on the left. The scale is in mm. The photograph is the same as one shown by Suo et al. (2024).

rim peak, also measured in the substrate level plane. For oblique impacts we use the same definitions but these two radii are functions of impact angle and azimuthal angle; $R_{rim}(\theta_I, \zeta)$ and $R_{cr}(\theta_I, \zeta)$.

The crater volume V_{cr} is the volume of the crater that lies below the surface level prior to impact. For normal impacts, we use a subscript n, giving crater radius $R_{cr,n}$, crater rim radius $R_{rim,n}$, and crater volume $V_{cr,n}$. Crater radii and volume for normal impacts along with dimensionless parameters π_R, π_V computed from these quantities are also listed in Table 1.

Crater scaling laws predict that a normal impact in the strength regime has crater radius

$$R_{cr,n}(\pi_3, \pi_4) = a_{pj} \left(\frac{4\pi}{3}\right)^{\frac{1}{3}} H_2 \pi_3^{-\frac{\mu}{2}} \pi_4^{-\nu}, \qquad (4)$$

and in the gravity regime

$$R_{cr,n}(\pi_2, \pi_4) = a_{pj} \left(\frac{4\pi}{3}\right)^{\frac{1}{3}} H_1 \pi_2^{-\frac{\mu}{2+\mu}} \pi_4^{-\frac{6\nu}{2+\mu}}, \qquad (5)$$

following Table 1 by Housen and Holsapple (2011), but with n subscripts to denote a normal impact. The parameters H_1, H_2 and exponents μ, ν are dimensionless but can depend upon the material properties (Housen et al., 2018).

A crater is in the strength regime if $\pi_3^{1+\mu/2} \pi_4^{\nu}/\pi_2 > 1$ (Housen and Holsapple, 2011). With exponents $\mu, \nu \sim 0.4$ typical of granular systems (Housen and Holsapple, 2011) and $Y_a = 500$ Pa, our experiments have $\pi_3^{1.2} \pi_4^{0.4}/\pi_2 \sim 1$, similar to unity. Our experiments lie near the line dividing strength and gravity regimes. Because we work in a granular system and its effective strength has not been measured, we often assume that we are in the gravity regime, following Housen and Holsapple (2011) who

suggested that impacts into granular systems would always be in the gravity regime. However, Scheeres et al. (2010) argued that even a low level of strength would put smaller and lower velocity impactors in a low gravity environment in the strength regime. Setting equation 4 or 5 equal to our normal impact crater radius and using values for the dimensionless parameters from Table 1, we estimate $H_1 \approx 0.6$ in the gravity regime or $H_2 \approx 0.7$ in the strength regime. These coefficients are similar to those estimated for different experiments (see Table 3 by Housen and Holsapple 2011).

We describe oblique impacts with impact angle θ_I which is the angle between the projectile velocity vector and the substrate plane. The impact angle is zero if the impact is grazing and is $\pi/2$ if the impact is normal to the surface, as shown in Figure 1a. The azimuthal angle ζ is measured using the site of impact as origin and in the plane perpendicular to the surface normal $\hat{\mathbf{n}}$ as shown in Figure 1b. We adopt the convention that $\zeta = 0$ in the uprange direction (opposite the $\hat{\mathbf{d}}$ vector), and toward the projectile launcher, following Raducan et al. (2022).

2.1. Ejecta mass at different azimuthal angles

We carried out a set of oblique impact experiments at different impact angles specifically to measure ejecta mass. To collect ejecta from our laboratory impacts, we constructed a set of eight nearly identical paper trays to catch ejecta. When placed next to each other, they cover an octagonal area around the impact site, as shown in Figure 2 and in the photo in Figure 3. Paper was used to keep the trays light, reducing compression of the sand substrate from the weight of the tray. Each paper tray weighs about 5.25 g. A circular area 8 cm in diameter, approximately matching crater diameter, was cut out from the apexes of the trays to allow ejecta to escape the impact

Table 2: Ejecta mass $M_{ej}(\theta_I, \zeta)d\zeta$ in g measured as a function of impact and azimuthal angles

θ_I/ζ	0	45	90	135	180	225	270	315
20	0.10±0.14	0.16±0.18	0.32±0.33	0.35±0.22	0.26±0.21	0.45±0.29	0.41±0.29	0.20±0.29
30	0.13±0.08	0.23±0.13	0.47±0.13	0.70±0.17	0.85±0.27	0.64±0.19	0.46±0.14	0.33±0.15
40	0.05±0.05	0.19±0.11	0.65±0.14	1.37±0.21	1.81±0.23	1.49±0.31	1.05±0.31	0.28±0.12
50	0.23±0.18	0.35±0.18	0.63±0.25	1.24±0.27	1.05±0.19	1.76±0.38	0.95±0.30	0.35±0.12
60	0.24±0.19	0.34±0.22	0.60±0.15	1.34±0.32	1.67±0.54	1.35±0.45	0.67±0.20	0.42±0.32
70	0.30±0.07	0.40±0.15	0.76±0.20	1.22±0.11	1.72±0.26	1.61±0.25	0.93±0.30	0.40±0.12
80	0.40±0.13	0.65±0.33	0.96±0.39	1.34±0.40	1.40±0.34	0.98±0.17	0.78±0.26	0.52±0.07

Each entry shows the ejecta mass in g as a function of azimuthal angle ζ and impact angle θ_I in trays of angular width $d\zeta = 45°$ as shown in Figure 2. Each row shows a single impact angle θ_I which is given in the leftmost column in degrees. The columns are headed by azimuthal angle ζ in degrees. Each entry gives the average of measurements from 6 experiments. The uncertainties show the standard deviation computed from the scatter of these measurements. An angle of $\zeta = 0$ corresponds to uprange (toward the projectile launcher).
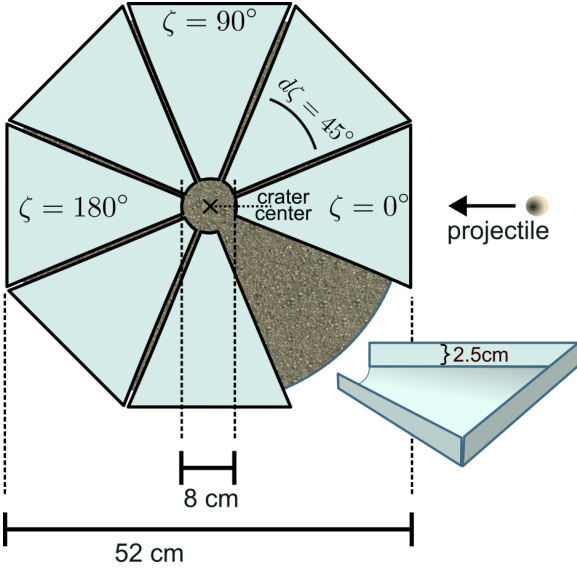

Figure 2: Orientation and shape of eight paper trays used to catch ejecta mass as seen from above. The projectile originates from the right. The crater center is centered in the central hole created by the paper trays. One of the paper trays is shown on the lower right with orientation chosen to show its folded edges.

Figure 3: A photograph of the trays covered in sand ejecta after an impact at $\theta_I = 60°$. The photo was taken from above. The green laser cross helps us aim the projectile and center the trays before impact. The projectile came from the right side and there is more ejecta in the downrange bins on the left.

region. Each tray covers an azimuthal angle of $d\zeta = 45°$, as illustrated in Figure 2. Each tray is labelled by its central azimuthal angle.

More ejecta mass originates at lower velocity near the crater rim than at higher velocity near the crater center (e.g., Housen et al. 1983). If a tray overlaps the crater rim, it would block the ejecta curtain. To capture the most ejecta mass, we designed the trays so that the tray inner edges are close to the crater rim, but do not cover it. In the mid-velocity regime of our 104 m/s impacts, craters are nearly round, with larger major to minor axis ratio at lower impact angles (at $\theta_I = 20°$, the major to minor crater axis ratio is only 1.18; see Table 5 by Suo et al. 2024). As a consequence, we cut the tray inner edges so that they are arcs of a circle. The three straight sides of the trays have folded edges, as shown on the lower right in Figure 2 so
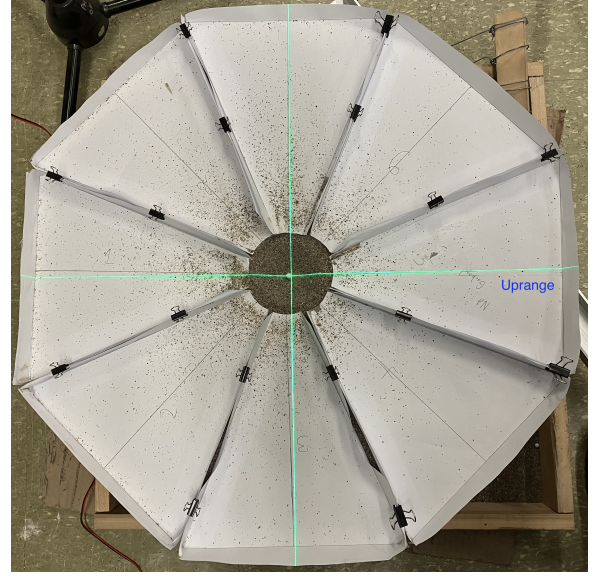
that ejecta does not bounce out just after impact or fall out when we move the tray to weigh it. The inner central curved tray edge is flat so that ejecta is not blocked by the tray. We aim the projectile so that the resulting crater is centered with respect to the central region of sand that is not covered by the trays, as illustrated in Figure 2. We did not use smaller trays because the ejecta mass collected in each tray is low, often less than a gram.

To improve projectile aim, we rebuilt the airsoft gun mount and digital servo trigger system so that it is held more securely than in our previous experiments. The airsoft gun is fired electronically without touching it. We also mounted an adjustable laser sight to an extension of the airsoft gun's picatinny rail which helps us aim the projectile and measure the impact angle. Prior to carrying out experiments with the trays, we do a set of impacts to ad-

4

just the airsoft gun tripod angle and location so that the crater is centered in the washtub container. The impact angle is measured with the laser sight and a large protractor that is drawn on a sheet of poster board, and is accurate to approximately 2 degrees.

Prior to each impact experiment, the surface is raked with a wire rake with wire tongs that are about 10 cm deep, as described in our prior experiments (Suo et al., 2024). After raking, the surface is leveled with a rectangular metal bar so that its level is equal to the height of the rim of the tub holding the sand. Afterward raking and leveling, the empty paper trays are placed on the surface with positions and orientations illustrated in Figure 2. After an impact we examine the crater. A few experiments were discarded because the crater rim did not lie within the central hole made by the trays. Otherwise, after each impact, the weight of the sand collected in each tray is measured with a digital scale.

We discuss uncertainties in our ejecta mass measurements. The distance from impact site to the center of the tray pattern gives a variation in the azimuthal angle (measured with origin at the impact site) subtended by each tray. Despite making improvements in our trigger servo system, we found that the site of impact is not exactly at the same position every time we fire a projectile. By examining crater locations with respect to a laser target, we find that the difference between desired and actual impact site has a standard deviation of about a cm. Ejecta scaling is done with origin at the impact site (Housen and Holsapple, 2011), as illustrated in Figure 1a, however, we attempted to center our trays with respect to the crater center, as illustrated in Figure 2. Craters from oblique impacts are not centered about the site of impact. To characterize the distance between crater center and impact site, Suo et al. (2024) measured the distance d_{ai} between the midpoint of uprange and downrange rim peaks and the site of impact. The distance d_{ai} is a maximum of 1.49 cm at impact angle $\theta_I = 40°$, and below 1.1 cm for the remaining impact angles, as listed in Table 5 by Suo et al. (2024). The crater at $\theta_I = 40°$ may be particularly elongated in part because the projectile passed through the ejecta curtain.

We consider the value $d_{ai} = 1.1$ cm (a value characteristic of our experiments for θ_I between 30 and 60°), the angle subtended by the $\zeta = 180°$ downrange tray at its inner edge is about 0.8 times $d\zeta = 45°$ and the angle subtended by the $\zeta = 0$ uprange tray is 1.4 times $d\zeta = 45°$. This implies that our ejecta masses are lower than they should be in the downrange trays and higher than they should be in the uprange trays. A similar size variation in angle subtended by the trays is caused when the impact site is 1 cm closer to the $\zeta = 90°$ tray than the 270° tray, in which case the trays on the closer side would receive more ejecta than the opposite side. The worst case error in subtended angle of about 40% seems large, however we find that the azimuthal variations in ejecta mass are so large that they dwarf uncertainties caused by errors in impact site with respect to the trays.

Because craters are smaller and more elongated at grazing angles, with $\theta \leq 30°$ the trays would miss ejecta near the crater rim, particularly along the crater minor axis at $\zeta \sim 90°$ and 270°. However, variations in ejecta mass caused by crater elongation are much smaller than those caused by craters that are not centered with respect to the trays. High velocity ejecta can land past the outer edge of our trays. At an impact angle $\theta_I = 40°$ we measured the fast ejecta mass that escaped our trays altogether, finding that it is at most 0.16 g and negligible.

We carried out 6 experiments at each of 7 impact angles ranging from 20 to 80° with an increment of 10°. The average ejecta masses in g (of 6 measurements) as a function impact angle and tray central azimuthal angle are listed in Table 2. Each panel in Figure 4 shows the ejecta masses in grams as a function of azimuthal angle ζ (along the horizontal axis) at a different impact angle. In Figure 4, the dotted lines show individual measurements from each experiment. The large dots at each azimuthal angle show the average ejecta masses computed from 6 experiments. The vertical error bars show the standard deviations computed from the scatter about the average values and are also listed in Table 2. The horizontal error bars in Figure 4 show the $d\zeta = 45°$ angle subtended by each tray.

Figure 4 shows that ejecta mass from oblique impacts depends on azimuthal angle, with more mass ejected in the downrange direction than in the uprange direction. At $\theta_I = 50°$, there is a dip in the ejecta mass at azimuthal angle $\zeta = 180°$, in the down range direction. At this impact angle, the projectile ricochets at a low angle, grazing the crater rim (see Figure 4 by Suo et al. 2024). The projectile itself could have blocked part of the ejecta curtain near $\zeta = 180°$, reducing the ejecta mass at this azimuthal angle.

Figure 4 shows that there is scatter in our ejecta mass measurements which can primarily be attributed to variations in impact location with respect to the tray pattern. Scatter can also be attributed to density variations within the sand (though we mitigated by raking the sand prior to impact), surface level variations of the sand prior to impact due to uneven leveling and disturbance caused by tray placement (less than about 1 mm), and relative variations (of order 0.3 cm) in tray locations and orientation (a few degrees) between experiments. We did not carry out experiments of ejecta mass at the grazing angle of $\theta_I = 10°$ because the crater is more elongated and smaller than at higher impact angles, and because it was more difficult to accurately aim the projectile at low impact angles.

Despite the scatter in individual measurements and the low mass of ejecta measured in each tray (often well below 1 g per bin), Figure 4 shows that azimuthal variations in ejecta mass are robustly measured in our experiments. The ratio between the ejecta mass in the downrange bin to that in the uprange bin is large, ranging from about 3 at $\theta_I = 80°$ to about 8 at $\theta_I = 50°$ (see Figure 7 below). The differences between up and downrange ejecta are so large that they exceed the errors introduced by centering

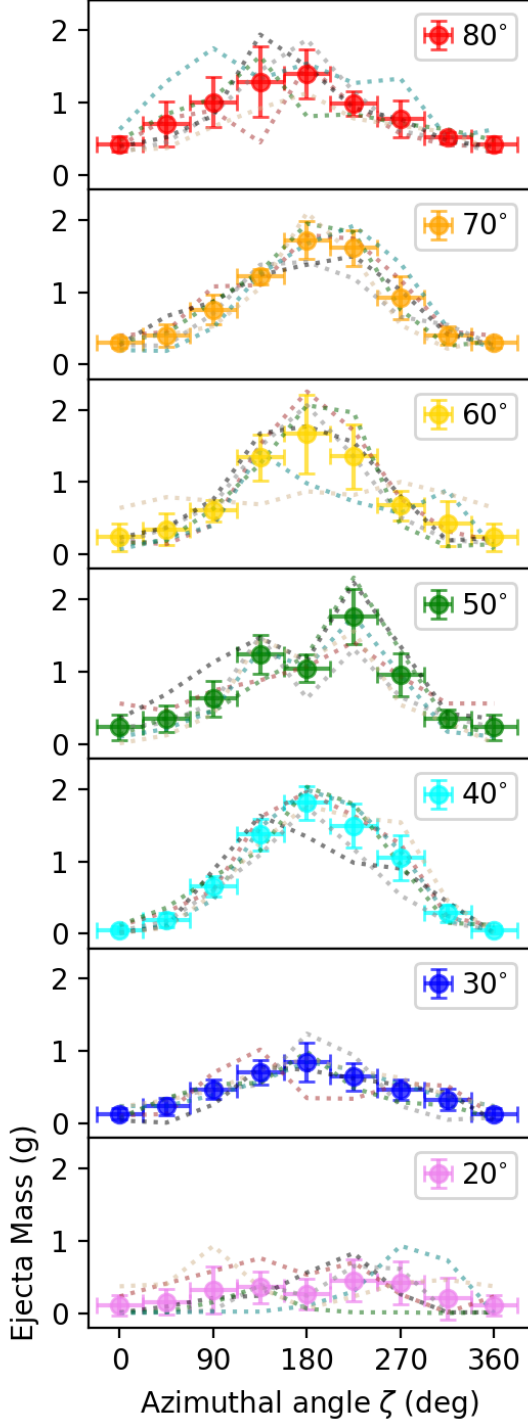the trays at the crater center rather than the impact site and by variations in impact location.

Figure 4: Mass in g per $d\zeta = 45°$ azimuthal bin measured at different impact angles. Dotted lines show individual experiments whereas dots show averages and vertical error bars show standard deviations computed from the scatter from different experiments at each azimuthal angle. The horizontal error bars show the tray angular widths.

Table 3: Total ejecta mass measured as a function of impact angle

θ_I (deg)	$M_{ej}(\theta_I)$ (g)
20	2.27 ± 0.93
30	3.81 ± 0.32
40	6.89 ± 0.75
50	6.57 ± 1.12
60	6.64 ± 0.70
70	7.35 ± 0.60
80	7.01 ± 1.41

Total ejecta mass in g as a function of impact angle. Each total ejecta masses is an average from 6 experiments. The uncertainty is the standard deviation computed from the scatter in the 6 experiments at each impact angle.

2.2. Total ejecta mass as a function of impact angle

Figure 5 shows total ejecta mass at each impact angle, θ_I. These are computed by summing the ejecta mass from the azimuthal bins. Black x's show total ejecta mass for each experiment and the large blue triangles show the averages computed from experiments at each impact angle. The vertical error bars are estimated from the scatter in the total ejecta mass measurements. The horizontal error bars represent uncertainty in impact angle. The ejecta mass measurements are in g and have axis on the left. Crater volume measurements are shown with orange circles, are in cm^3, and have axis on the right. Crater volume measurements are taken from Table 5 by Suo et al. (2024) except that at $\theta_I = 80°$ which we corrected after reexamining the crater profile.

Figure 5 shows that the total mass in ejecta is approximately proportional to crater volume, as expected from prior studies (Housen et al., 1983; Luther et al., 2018). The low ejecta mass at grazing impact angles (lower than 50°) is related to the reduction in crater volume that was previously noted by Suo et al. (2024) and that was attributed to energy carried away via ricochet of the projectile. A crater mass can be estimated from the product of crater volume times substrate density; $M_{cr} = \rho_a V_{cr}$. Crater mass is the mass that was originally located inside the crater. In Figure 5 we have adjusted the y-axis scales so that crater volume measurements lie on top of crater ejecta mass measurements, giving ratio of ejecta to crater mass

$$\frac{M_{ej}(\theta_I)}{M_{cr}(\theta_I)} \approx 0.35. \qquad (6)$$

The shock physics code impact simulations by Luther et al. (2018) predict a ratio of ejecta to crater mass of 0.37 for their high velocity impacts (see their Figure 15) with a lower value of 0.25 for their lowest impact velocity (1 km/s) simulation. Our value of 0.35 is consistent with this prediction, despite the difference in impact regime (our impact velocity is at least an order of magnitude lower). In hypervelocity experiments into layered sand Stoeffler et al. (1975) attributed the relatively large value of crater mass
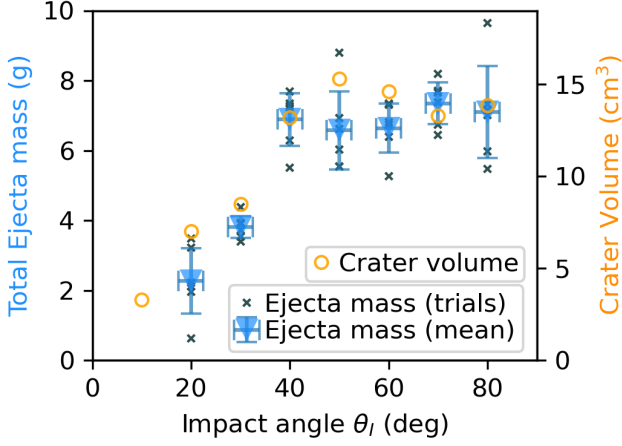
Figure 5: Total ejecta mass and ejecta volume measured at each impact angle. Black x's show the ejecta mass measurements for each individual experiment, and blue triangles show the means of these measurements, with axis on the left. Crater volume measurements are shown with orange circles and with axis on the right.

compared to ejecta mass to compactification of the substrate and deformation associated with radial expansion and rim uplift (which exceeds ejecta curtain depth Sharpton 2014; Sturm et al. 2016; Neiderbach et al. 2023). Our low value of ejecta to crater mass does not necessarily imply that our experiments fail to capture most of the ejecta, even though our trays do not capture some low velocity material ejected very near the crater rim.

3. Crater radii as a function of azimuthal angle

Models for the ejecta velocity and mass distribution can relate the properties of the ejecta curtain to the crater radius (Housen and Holsapple, 2011). However, for oblique impacts, the crater radius depends on both impact and azimuthal angles. To relate our measurements of the azimuthal ejecta mass distribution to models for the ejecta curtain we first measure the crater radius as a function of impact and azimuthal angles.

Suo et al. (2024) measured crater depth profiles for oblique impacts by taking a video while slowly stepping a line-laser across the crater. The videos were processed to measure crater depth as a function of position at 8 different impact angles and creating eight two dimensional crater depth arrays (Suo et al., 2024). Here we analyze these eight crater depth profiles again but to measure crater and rim radius as a function of azimuthal and impact angles.

Suo et al. (2024) measured crater depth profiles from 8 experiments, at impact angles ranging from $\theta_I = 10°$ to $80°$ in increments of $10°$. For each of the eight computed two dimensional crater depth arrays, we extracted the depth as a function of distance from the site of impact at different azimuthal angles. Positions along a desired angle ζ were extracted using linear interpolation from the 2d-arrays depth arrays. The depth profiles at each azimuthal angle were smoothed using a 1 dimensional Savinsky-Golay
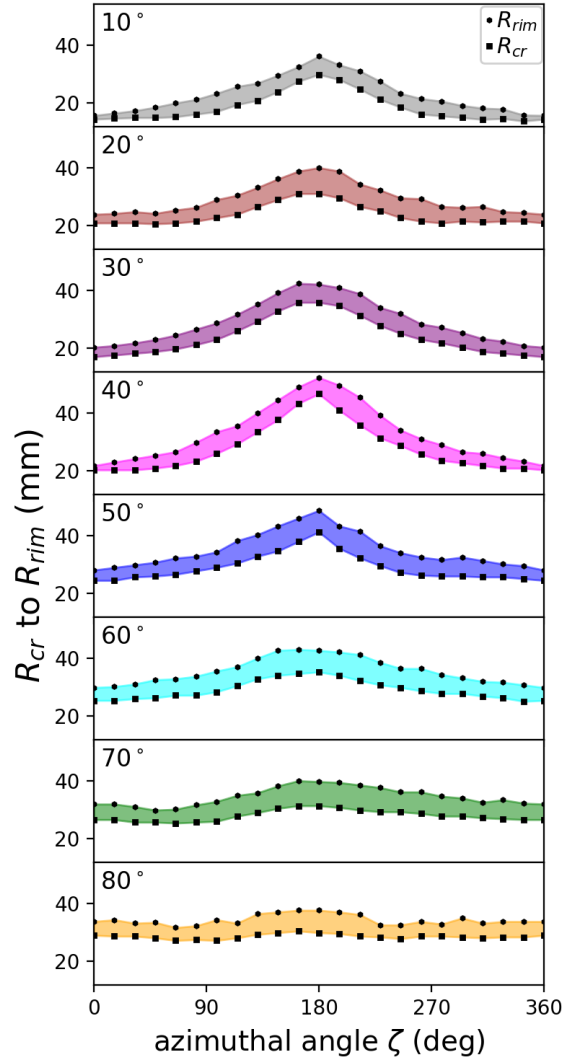

Figure 6: Radius of rim peak, R_{rim} and R_{cr} as a function of impact angle θ_I and azimuthal angle ζ. These are measured from the crater depth profiles obtained by Suo et al. (2024). In each panel we plot measurements at a different impact angle θ_I which is labeled in degrees on the top left of each panel. The horizontal axis is the azimuthal angle ζ. Rim peak R_{rim} radii in mm from the site of impact are shown with the black circles and R_{cr} (the radii at which the crater depth is equal to the substrate level prior to impact) in mm are shown with black squares. The regions between the rim and R_{cr} values are filled with color. The shallowest grazing impact is shown in the top panel.

filter of window length 3 mm and polynomial order 3. The maximum height along the smoothed profile gave the radius of the rim peak $R_{rim}(\theta_I, \zeta)$. Within the rim we identified the radius which was at the same depth as the undisturbed surface prior to impact, $R_{cr}(\theta_I, \zeta)$. The resulting rim and level crossing radii are plotted in Figure 6 as a function of azimuthal angle for each of 8 impact angles θ_I.

The rim diameter and crater diameter for a normal impact listed in Table 1 we computed from the medians of the rim radii and the medians of the crater radii at different azimuthal angles using the depth profile from the

experiment at an impact angle of $\theta_I = 80°$. Twice the rim radius differs slightly from the rim to rim crater diameter along the major axis of 7.1 cm previously listed in Table 5 by Suo et al. (2024). We give an updated value for crater volume in Table 1 for a normal impact based on the same depth profile as we suspect that there was a minor error in the value reported in Table 5 by Suo et al. (2024).

The size of azimuthal variations in ejecta mass exceed those in crater radius. To show this, we examine the ratio of ejecta mass in the downrange direction to that in the uprange direction and we compare this ratio to the ratio of the downrange crater radius to uprange crater radius. in cigure 7 at each impact angle, black dots show the ratio of the maximum ejecta mass to the minimum ejecta mass using the average values plotted in Figure 4. The maximum values tend to be downrange and the minimum values uprange. At each impact angle, with red squares, we show the ratio of the maximum to minimum crater radii that are also shown in Figure 6. Figure 7 shows that the ejecta mass amplitudes of azimuthal variation are higher than the amplitudes of azimuthal variation in the crater radius.

Figure 7 shows that the uprange/downrange asymmetry in ejecta mass is large. Due to the placement of our ejecta trays (centered at crater center rather than impact point), the asymmetry could be even larger. If we correct by the extreme error values estimated in section 2.1), the ratio of maximum to minimum ejecta mass could increase by a factor as large as $1.4/0.8 = 1.7$.
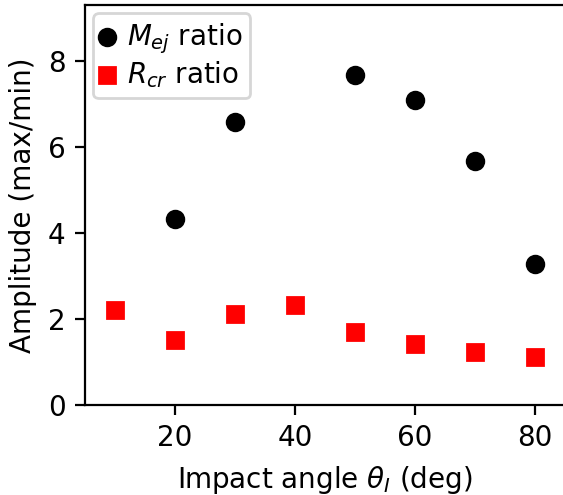

Figure 7: Amplitudes of azimuthal variation in ejecta mass and crater radius as a function of impact angle. With black squares we plot the ratio of the maximum to minimum ejecta mass from the different azimuthal bins using the means from 6 experimental trials at each impact angle. The red dots show the ratio of the maximum to minimum crater radius at each impact angle. The maximum values are downrange and the minimum values are uprange. We do not plot the mass ratio at $\theta_I = 40°$ because the uprange bin had very low mean ejecta mass, giving a ratio above 20. The azimuthal variations in ejecta curtain mass are larger than azimuthal variations in crater radius.

3.1. Fitting the crater radius as a function of impact and azimuthal angles

Using least-square minimization we fit a function to the radii $R_{cr}(\theta_I, \zeta)$ and $R_{rim}(\theta_I, \zeta)$ that we measured from the crater depth profiles. The function we choose extends the function for crater radius adopted by Raducan et al. (2022) that is linear in impact angle θ_I and depends on $\cos \zeta$. We use the function

$$R(\theta_I, \zeta) = a_{00} + \sum_{j=1}^{2} \sum_{k=0}^{2} a_{jk} \left(\theta_I - \frac{\pi}{2} \right)^j (\cos \zeta)^k \qquad (7)$$

with coefficients a_{00} and a_{jk} with integers $j > 0$ and $k \geq 0$. For the fit to R_{cr}, the coefficient $a_{00} = R_{cr,n}$ for a normal impact. We found that a polynomial function in θ_I required fewer coefficients for the same quality of fit (as measured from the reduced χ^2) than one that only contained trigonometric functions of θ_I. A least squares fitting routine in python (`scipy.optimize.least_squares` with the Trust Region Reflective algorithm) was used to find the coefficients a_{ij} that minimize χ^2. Uncertainties for each coefficient are 1σ errors that are estimated from the diagonals of the covariance matrix and using the variance of the residuals as an estimate for the standard deviation of each data point. The best fitting coefficients (via equation 7) for our measurements of R_{cr} and R_{rim} (shown in Figure 6) are listed in Table 4 along with the standard deviation of the residuals. in Figure 8 the best fitting functions are shown in the top panels with measurements in the middle panels and residuals (data subtracted by model) shown in the bottom panels. Figure 8a shows our fit to R_{cr} measurements, and Figure 8b shows our fit to R_{rim} measurements in both cases fit varying all 6 coefficients in equation 7.

In Figure 9 the colored dots show the crater radii ($R_{cr}(\theta_I, \zeta)$) we measured as seen from above the surface. Here the $+x$ axis is in the uprange direction. Dot size and color depend upon impact angle. In Figure 9a we plot the best fitting function (with coefficients for equation 7 and coefficients in the column labelled R_{cr} in Table 4 for each impact angle with lines, and with line color matching the dots at the same impact angle.

Figure 8a and Figure 9a show that our fitting function (equation 7) matches our measurements for the crater radius fairly well. The largest residual errors are at impact angle $\theta_I = 40°$. The elongation of the crater along the downrange direction at this impact angle can in part be attributed to the ricochet of the projectile that grazed the crater rim along the negative x axis downrange of impact (Suo et al., 2024).

Raducan et al. (2022) fit the crater radii of their impact simulations with a function (their equation 9) similar to equation 7, dependent upon azimuthal and impact angle, but only containing the two coefficients $a_{00} = R_{cr,n}$ and $a_{11} = -R_{cr,n}\frac{1}{2}\frac{1}{100}\frac{180}{\pi} = -0.29 R_{cr,n}$. In Figure 8c we show a least-square model that minimizes a version of the function in equation 7 containing only two free parameters, a_{00} and a_{11}. The resulting best fit two coefficient
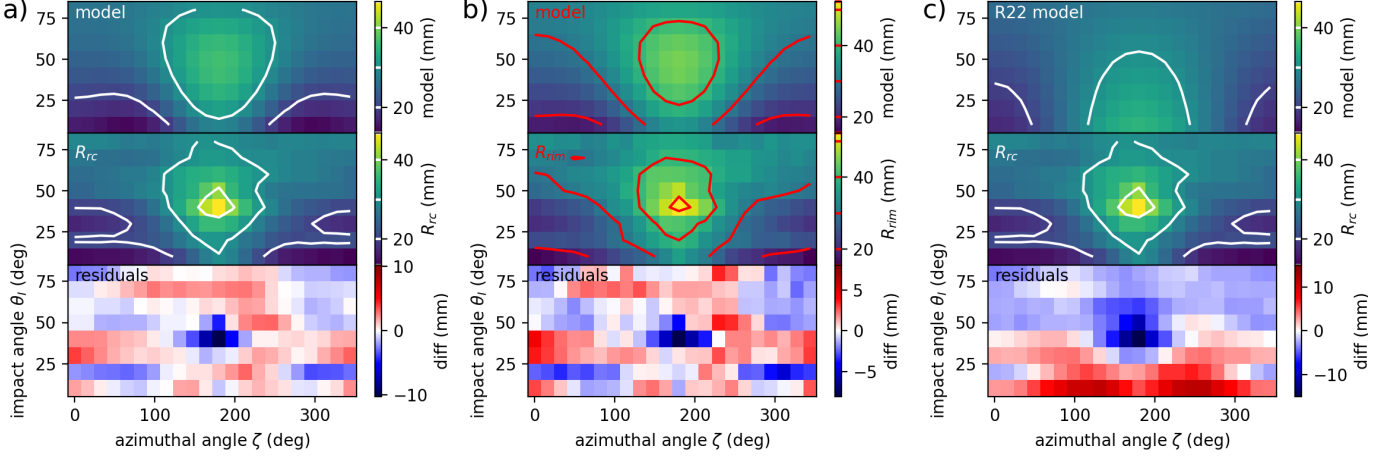
Figure 8: Results of least-squares fitting to crater radius as a function of azimuthal angle and impact angle. The x-axis is azimuthal angle ζ in degrees and the y-axes are impact angle θ_I in degrees. The color bars are in mm. a) The top panel shows the model of equation 7 fit to our measurements for the radius $R_{cr}(\theta_I, \zeta)$. The middle panel shows our measurements. These are the same as shown in Figure 6 but illustrated as a two-dimensional image. The bottom panel shows the residuals, model subtracted by data measurements. b) Similar to a) except the model of equation 7 is fit to measurements of the rim radius R_{rim}. c) Similar to a) except the model only contains 2 coefficients, a_{00} and a_{11} (following equation 9 by Raducan et al. 2022).

Table 4: Fits to crater radius

Fit to coeffs.	R_{cr} (mm)	R_{rim} (mm)	R_{cr} (R22) (mm)
a_{00}	26.12 ± 0.58	32.11 ± 0.60	26.07 ± 0.33
a_{10}	12.28 ± 1.70	13.76 ± 1.74	
a_{20}	-12.47 ± 1.05	-14.19 ± 1.08	
a_{11}	-13.64 ± 0.95	-18.24 ± 0.98	-6.36 ± 0.53
a_{21}	6.56 ± 0.83	8.89 ± 0.86	
a_{12}	2.43 ± 0.24	2.09 ± 0.24	
Residuals	1.92	1.97	4.35
Figures	8a,9a	8b	8c,9b

Notes: The R_{cr} column lists coefficients of the function in Equation 7 resulting from least-squares minimization fitting of our measured values for R_{cr}, shown in Figure 6. The R_{rim} column is similar but for fits to our measured rim radii. The column labelled R_{cr} (R22) shows coefficients from a fit which only used two coefficients a_{00}, a_{11} following the function for R_{cr} adopted by Raducan et al. (2022) (their equation 9). The row denoted residuals list the standard deviation of the residuals in mm. The last row shows the figures in which measurements, model and residuals are displayed.

model and residuals are shown in Figure 8c. The values of the two coefficients for this fit are listed in the rightmost column in Table 4. The coefficients of our best fit two coefficient model has a ratio of $a_{11}/a_{00} = -0.24$ which is similar to the value of -0.29 of the model by Raducan et al. (2022) (their equation 9). The residuals between the two-component model and our measurements are higher for the two coefficient model than that with six coefficients, as would be expected since fewer free parameters are varied in the χ^2 minimization. Residuals between our measurements and the two-component model are primarily high at

low impact angle where our crater radii are smaller than at higher impact angle. Figure 9b, where we show the crater shapes predicted by the two-component model (as dashed lines) along with our crater shapes (shown with dots), also shows that our measured crater radii are smaller than predicted by the two-component model at low impact angle.

The impact simulations by Raducan et al. (2022) were of a 7 km/s impact. The function used by Raducan et al. (2022) does not have a smaller crater at low impact angles, which was true of our experiments. Craters are smaller because impact energy and momentum was carried away by the projectile during ricochet at grazing impact angles in our lower velocity experiments (Suo et al., 2024). The simulations by Raducan et al. (2022) were of a high velocity (7 km/s) impact which would have been more likely to melt or vaporize the projectile than cause it to ricochet. The two component function fit by Raducan et al. (2022) to their simulated impacts for crater radius as a function of azimuthal and impact angle was close to the radii we measured (particularly at impact angles greater than 40°) despite the difference in impact regime.

4. Crater ejecta distribution models

The ejecta model for normal impacts by Housen and Holsapple (2011) assumes that the velocity and mass distributions for most of the ejecta are independent of projectile radius. This assumption is described as the "point source approximation". Ejecta velocity and mass is a power law function of x, the distance between ejecta launch site and impact site. The power law functions are approximately truncated at an inner radius that is approximately equal to the projectile radius a_{pj} and outer radius that is approximately equal to the crater radius R_{cr}, as illustrated
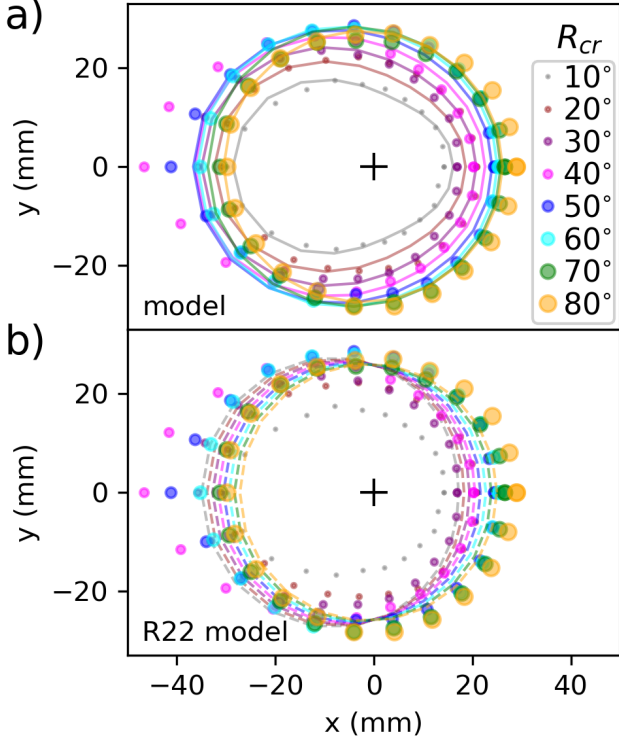
Figure 9: a) Circles show crater radius $R_{cr}(\theta_I, \zeta)$ measured from crater profiles and as seen from above the surface. Each impact angle is shown with different color and size markers. The model, described by equation 7, has coefficients listed in the column labelled R_{cr} in Table 4 and is shown with solid lines. At each impact angle, the line color for the model matches that of the measurements that are shown with dots. The impact site is marked with a black cross. The projectile originated from the $+x$ direction. b) Similar to a) except the colored dashed lines show a two coefficient fit to the crater radius (folowing Raducan et al. 2022) and with coefficients listed in the column labelled R_{cr}(R22) in Table 4.

in Figure 9.

The ejecta scaling model by Housen and Holsapple (2011) has total mass ejected at all positions up to x from the site of impact

$$M_{ej,n}(<x) = k_n \rho_a (x^3 - n_1 a_{pj}^3) \quad \text{for} \quad n_1 a_{pj} < x < n_2 R_{cr,n}. \tag{8}$$

This power law form for the ejecta mass distribution is illustrated in Figure 10. The parameter k_n is dimensionless but can depend upon the material properties (Housen et al., 2018). Housen and Holsapple (2011) found that parameters $n_1 \approx 1.2$ and $n_2 \approx 1$.

Following Raducan et al. (2022), we modify the coefficients used in the crater ejecta scaling laws by Housen and Holsapple (2011) to become functions of impact and azimuthal angles θ_I, ζ. We modify equation 8 to consider the ejecta mass in an azimuthal bin of size $d\zeta$ in radians

$$dM_{ej}(<x, \theta_I, \zeta)d\zeta = \frac{\rho_a}{2\pi} k(\theta_I, \zeta)(x^3 - n_1 a_{pj}^3)d\zeta$$
$$\text{for} \quad n_1 a_{pj} < x < n_2 R_{cr}(\theta_I, \zeta). \tag{9}$$
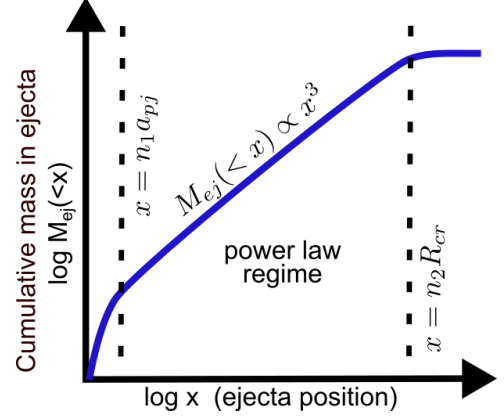

Figure 10: Illustrating the point source approximation by Housen and Holsapple (2011) for the cumulative ejecta mass distribution and the region where power-law scaling applies.

The factor of 2π arises because the total ejecta mass is found by integrating over the azimuthal angle ζ. The function $k(\theta_I, \zeta)$ has limit

$$\lim_{\theta_I \to \pi/2} k(\theta_I, \zeta) = k_n \tag{10}$$

where k_n is the coefficient for a normal impact in equation 8. The crater radius is dependent upon azimuthal and impact angles and

$$\lim_{\theta_I \to \pi/2} R_{cr}(\theta_I, \zeta) = R_{cr,n} \tag{11}$$

where $R_{cr,n}$ is the crater radius for a normal impact in equation 5. We assume that coefficients n_1 and n_2 are independent of impact and azimuthal angle.

The total ejecta mass (integrated out to the crater radius) in an azimuthal bin of width $d\zeta$ in radians is

$$dM_{ej}(\theta_I, \zeta) \approx \frac{\rho_a}{2\pi} k(\theta_I, \zeta) R_{cr}^3(\theta_I, \zeta)d\zeta \tag{12}$$

where we have used $n_2 \approx 1$ found by Housen and Holsapple (2011) in equation 9 for the maximum value of ejecta radius and assumed that crater radius is much larger than the projectile radius; $R_{cr,n} \gg a_{pj}$.

For the function $k(\theta_I, \zeta)$, we adopt a form for the function;

$$k(\theta_I, \zeta) = k_n + k_1 \cos\theta_I \cos\zeta. \tag{13}$$

Using equation 12 and parameters based on our model for $R_{cr}(\theta_I, \zeta)$ (described in section 3.1) we fit k_n and k_1 to the mean ejecta mass we measured as a function of impact and azimuthal angle. The averages at each impact angle consistent of mean values from measurements of 6 experiments per impact angle and at each of 8 possible azimuthal bins. Our least-squares minimizing fitting procedure is the same as described in section 3.1. The model that minimizes χ^2 is shown in Figure 11. Best fitting parameters for the function in equation 13 are

$$k_n = 0.19 \pm 0.01 \text{ g}$$
$$k_1 = 0.02 \pm 0.02 \text{ g} \tag{14}$$

with a standard deviation of 0.28 g in the residuals (model subtracted by measurements) that are shown in the bottom panel in Figure 11.

Our best fitting value for k_n is at the lower end of the range 0.2 to 0.5 for normal impacts into substrate materials inferred by Housen and Holsapple (2011) via comparison of their ejecta scaling model to experimental measurements. Our trays do not catch all the lowest velocity ejecta, which may in part account for our low k_n value.

Our best fitting value for k_1 is near zero, which implies that the function $k(\theta_I, \zeta)$ is only weakly dependent upon impact and azimuthal angles. Variations in the total ejecta mass (integrated in ejection launch position x) as a function of azimuthal angle in equation 12 are primarily due to the sensitivity of the crater radius to impact and azimuthal angles.

The function used by Raducan et al. (2022) to describe azimuthal variations in the ejecta mass, $k(\theta_I, \zeta) = \frac{k_n}{2\pi} \exp\left[-0.02\cos(\zeta)\cos(\theta_I)\right]$ (their equation 8, which we have modified to be per bin in ζ). This function is weakly dependent upon impact and azimuthal angles. Our measurements of the ejecta mass azimuthal mass distribution confirm this weak dependence. We suspect that Figure 12c by Raducan et al. (2022) is probably not showing their function $k(\theta_I, \zeta)$ (given in their equation 8) as the plotted function is more sensitive to azimuthal and impact angles than predicted by their function. Figures 12a, b and d by Raducan et al. (2022) may have flipped or mislabelled x-axes as the plotted functions appear inconsistent with their equations 6, 7 and 9. Our experimental measurements are in agreement with two of the functions proposed by Raducan et al. (2022); their equation 8 (for $k(\theta_I, \zeta)$) and their equation 12 (for $R_{cr}(\theta_I, \zeta)$), despite some confusion caused by their Figure 12.

5. Discussion and Summary

In this study we have measured the azimuthal ejecta mass distribution for intermediate (~ 104 m/s) velocity oblique impacts into sand. Our measurements extend our characterization of the intermediate velocity regime for oblique impacts in a granular system, building upon the experimental study by Suo et al. (2024). Using paper trays to catch ejecta, we have measured the azimuthal ejecta mass distribution as a function of impact angle. Even though craters are nearly round, the ejecta curtains are strongly asymmetrical, with more ejecta launched in the downrange than uprange direction, confirming the study by Hessen et al. (2007). The ratio of ejecta mass in the downrange bin to the uprange one is large and ranges from about 3 at an impact angle of $\theta_I = 80°$ to at least 8 at an impact angle of $\theta_I = 40°$. The large ejecta mass in the downrange direction is consistent with the strong, high amplitude subsurface pulses on the downrange side measured with embedded accelerometers by Suo et al. (2024).

Crater rims from oblique impacts are not centered about the site of impact. Using crater depth profiles measured
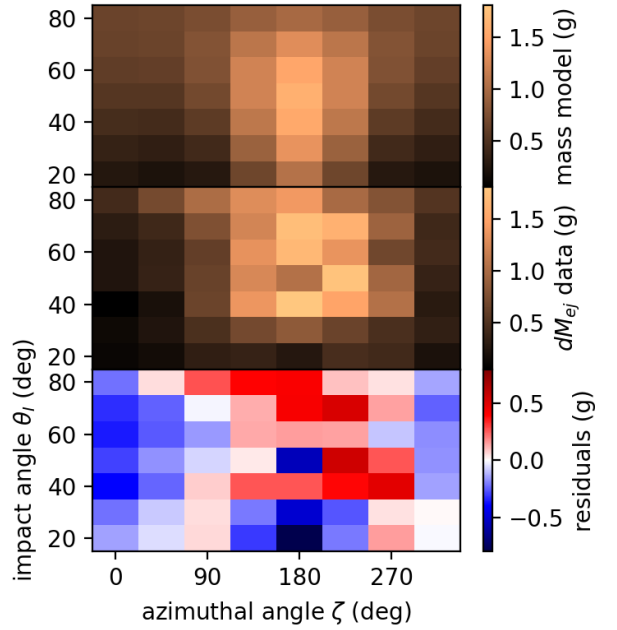

Figure 11: Ejecta mass as a function of impact and azimuthal angle. The top panel shows the best fit model from equation 12 with function equation 13 for the function $k(\theta_I, \zeta)$ and parameters in equation 14. The model uses crater radius model for $R_{cr}(\theta_I, \zeta)$ discussed in section 3.1 and shown in Figure 8. The middle panel shows the measurements of ejecta mass in 45° wide azimuthal bins. Each pixel consists of an average of 6 experimental data points. The bottom panel shows residuals (data subtracted by model).

by Suo et al. (2024) we have measured the crater radius $R_{cr}(\theta_I, \zeta)$ (a distance from the site of impact illustrated in Figure 1a), as a function of impact and azimuthal angles. We find that the azimuthal ejecta mass distribution is approximately proportional to the cube of crater radius $R_{cr}(\theta_I, \zeta)$. This implies that the function $k(\theta_I, \zeta)$ (defined in equation 9), is approximately constant. The insensitivity of the function $k(\theta_I, \zeta)$ describing the ejecta mass distribution to impact and azimuthal angles would facilitate computing quantities associated with the cumulative affects of impacts on small bodies, including angular momentum drain (Dobrovolskis and Burns, 1984) and erosion (Quillen et al., 2024).

The shape of subsurface pulses measured by Suo et al. (2024) from accelerometers at the particular subsurface locations were remarkably similar for oblique impacts at different impact angles (see their Figure 17). Suo et al. (2024) suggested that it might be possible to describe the subsurface pulses and the resulting ejecta velocity field by rescaling the amplitude of the velocity field. Our finding, that the ejecta mass azimuthal distribution depends primarily on crater radius, supports this proposal. There may be a way to characterize ejecta distribution and impact generated subsurface motions via an angular and time dependent function that also gives $R_{cr}(\zeta, \theta)$.

Raducan et al. (2022) modified ejecta scaling laws to describe simulated oblique impacts with four angular de-

pendent functions. We have experimentally characterized two of these functions: crater radius $R_{cr}(\theta_I, \zeta)$ and the function $k(\theta_I, \zeta)$ (defined in equation 9), though in a lower velocity regime and for a granular substrate, sand. Our angular dependent functions for crater radius and $k(\theta_I, \zeta)$ describing the ejecta mass distribution are remarkably similar to those presented by Raducan et al. (2022).

We found that the azimuthal asymmetry in ejecta mass was so large that we could detect it with unsophisticated impact experiments. The biggest source of error in our experiments is likely is due to variations in projectile aim. Impact experiments with more accurate targeting could confirm and improve upon our measurements and study the ejecta mass distribution from oblique impacts at different impact velocities. In future work, we also hope to experimentally characterize two additional functions of impact and azimuthal angles, θ_I and ζ, for the coefficient C_1 and exponent μ used by Housen and Holsapple (2011) to describe the ejecta velocity as a function of ejecta launch position. We would also like to characterize functions describing angular variations in ejecta angle as ejecta angle is also sensitive to azimuthal and impact angles and ejecta launch position (Anderson et al., 2004; Raducan et al., 2022; Suo et al., 2024).

Data availability: The data that support the findings of this study and code used to generate all figures in this manuscript are openly available at `https://github.com/aquillen/azimuthal_mass`.

References

Anderson, J., Schultz, P.H., 2006. Flow-field center migration during vertical and oblique impacts. International Journal of Impact Engineering 33, 35–44.

Anderson, J.L.B., Schultz, P.H., Heineck, J.T., 2003. Asymmetry of ejecta flow during oblique impacts using three-dimensional particle image velocimetry. Journal of Geophysical Research (Planets) 108, 5094. doi:10.1029/2003JE002075.

Anderson, J.L.B., Schultz, P.H., Heineck, J.T., 2004. Experimental ejection angles for oblique impacts: Implications for the subsurface flow-field. Meteoritics & Planetary Science 39, 303–320. doi:10.1111/j.1945-5100.2004.tb00342.x.

Brisset, J., Sánchez, P., Cox, C., Corraliza, D., Hatchitt, J., Madison, A., Miletich, T., 2022. Asteroid regolith strength: Role of grain size and surface properties. Planetary and Space Science 220, 105533. doi:10.1016/j.pss.2022.105533.

Campo Bagatin, A., Farinella, P., Petit, J.M., 1994. Fragment ejection velocities and the collisional evolution of asteroids. Planary and Space Science 42, 1099–1107. doi:10.1016/0032-0633(94)90010-8.

Çelic, O., Ballouz, R.L., Scheeres, D.L., Kawakatsu, Y., 2022. A numerical simulation approach to the crater-scaling relationships in low-speed impacts under microgravity. Icarus 377, 114882.

Cheng, A.F., Michel, P., Jutzi, M., Rivkin, A., Stickle, A., Barnouin, O., Ernst, C., Atchison, J., Pravec, P., Richardson, D., team, A., team, A., 2016. Asteroid impact & deflection assessment mission: Kinetic Impactor. Planetary and Space Science 121, 27–35.

Dobrovolskis, A.R., Burns, J.A., 1984. Angular momentum drain: A mechanism for despinning asteroids. Icarus 57, 464–476. URL: https://www.sciencedirect.com/science/article/pii/0019103584901301, doi:https://doi.org/10.1016/0019-1035(84)90130-1.

Farinella, P., Davis, D.R., Paolicchi, P., Cellino, A., Zappala, V., 1992. Asteroid collisional evolution - an integrated model for the evolution of asteroid rotation rates. Astronomy & Astrophysics 253, 604–614.

Greenstreet, S., Gladman, B., McKinnon, W.B., Kavelaars, J.J., Singer, K.N., 2019. Crater Density Predictions for New Horizons Flyby Target 2014 MU69. Astrophysical Journal Letters 872, L5. doi:10.3847/2041-8213/ab01db, arXiv:1812.09785.

Hessen, K.K., Herrick, R.R., Yamamoto, S., Barnouin-Jha, O.S., Sugita, S., Matsui, T., 2007. Low-Velocity Oblique Impact Experiments in a Vacuum, in: 38th Annual Lunar and Planetary Science Conference, p. 2141.

Holsapple, K.A., 1993. The scaling of impact processes in planetary sciences. Annual Review of Earth and Planetary Sciences 21, 333–373.

Holsapple, K.A., Housen, K.R., 2012. Momentum transfer in asteroid impacts. i. theory and scaling. Icarus 221, 875–887.

Housen, K., Sweet, W., Holsapple, K.A., 2018. Impacts into porous asteroids. Icarus 300, 72–96.

Housen, K.R., Holsapple, K.A., 2011. Ejecta from impact craters. Icarus 211, 856–875.

Housen, K.R., Schmidt, R.M., Holsapple, K.A., 1983. Crater ejecta scaling laws: Fundamental forms based on dimensional analysis. J. Geophys. Res. 88, 2485–2499.

Jutzi, M., Michel, P., 2014. Hypervelocity impacts on asteroids and momentum transfer. i. numerical simulations using porous targets. Icarus 229, 247–253.

Luther, R., Zhu, M.H., Collins, G., Wünnemann, K., 2018. Effect of target properties and impact velocity on ejection dynamics and ejecta deposition. Meteoritics & Planetary Science 53, 1705–1732. doi:10.1111/maps.13143.

Mazur, R., Beczek, K., Janiszewski, J., Koperski, W., Polakowski, C., Fikus, B., Sochan, A., Woźniak, R., Goździk, D., Ryżak, M., Bańda, M., Bieganowski, A., 2022. Experimental investigations of crater formation as a result of high-velocity impacts on sand bed. PLoS ONE 17, e0265546. doi:10.1371/journal.pone.0265546.

Melosh, J., Pierazzo, E., 2000. Understanding oblique impacts from experiments, observations, and modeling. Annu. Rev. Earth Planet. Sci. , 141–167.

Neiderbach, M., Suo, B., Wright, E., Quillen, A., Lee, M., Miklavcic, P., Askari, H., Sánchez, P., 2023. Surface particle motions excited by a low velocity normal impact into a granular medium. Icarus 390, 115301.

Quillen, A.C., Luniewski, S., Rubinstein, A.E., Couturier, J., Glade, R., Nakajima, M., 2024. Wind erosion and transport on planetesimals. Icarus 411, 115948. doi:10.1016/j.icarus.2024.115948, arXiv:2310.09572.

Raducan, S.D., Davison, T.M., Collins, G.S., 2022. Ejecta distribution and momentum transfer from oblique impacts on asteroid surfaces. Icarus 374, 114793. doi:10.1016/j.icarus.2021.114793, arXiv:2105.01474.

Scheeres, D.J., Hartzell, C.M., Sánchez, P., Swift, M., 2010. Scaling forces to asteroid surfaces: The role of cohesion. Icarus 210, 968–984. doi:10.1016/j.icarus.2010.07.009, arXiv:1002.2478.

Sharpton, V.L., 2014. Outcrops on lunar crater rims: Implications for rim construction mechanisms, ejecta volumes and excavation depths. J. Geophys. Res. Planets 119, 154–168.

Stoeffler, D., Gault, D.E., Wedekind, J., Polkowski, G., 1975. Experimental hypervelocity impact into quartz sand: Distribution and shock metamorphism of ejecta. Journal of Geophysical Research 80, 4062–4077. doi:10.1029/JB080i029p04062.

Sturm, S., Kenkmann, T., Hergarten, S., 2016. Ejecta thickness and structural rim uplift measurements of Martian impact craters: implications for the rim formation of complex impact craters. J. Geophys. Res. 121, 1026–1053.

Suo, B., Quillen, A.C., Neiderbach, M., O'Brient, L., Miakhel, A.S., Skerrett, N., Couturier, J., Lherm, V., Wang, J., Askari, H., Wright, E., Sánchez, P., 2024. Subsurface pulse, crater and ejecta asymmetry from oblique impacts into granular media. Icarus 408,

115816. doi:10.1016/j.icarus.2023.115816, arXiv:2308.01876.

Thomas, C.A., Naidu, S.P., Scheirich, P., Moskovitz, N.A., Pravec, P., Chesley, S.R., Rivkin, A.S., Osip, D.J., Lister, T.A., Benner, L.A.M., Brozović, M., Contreras, C., Morrell, N., Rożek, A., Kušnirák, P., Hornoch, K., Mages, D., Taylor, P.A., Seymour, A.D., Snodgrass, C., Jørgensen, U.G., Dominik, M., Skiff, B., Polakis, T., Knight, M.M., Farnham, T.L., Giorgini, J.D., Rush, B., Bellerose, J., Salas, P., Armentrout, W.P., Watts, G., Busch, M.W., Chatelain, J., Gomez, E., Greenstreet, S., Phillips, L., Bonavita, M., Burgdorf, M.J., Khalouei, E., Longa-Peña, P., Rabus, M., Sajadian, S., Chabot, N.L., Cheng, A.F., Ryan, W.H., Ryan, E.V., Holt, C.E., Agrusa, H.F., 2023. Orbital period change of Dimorphos due to the DART kinetic impact. Nature 616, 448–451. doi:10.1038/s41586-023-05805-2, arXiv:2303.02077.

Tsujido, S., Arakawa, M., Suzuki, A.I., Yasui, M., 2015. Ejecta velocity distribution of impact craters formed on quartz sand: Effect of projectile density on crater scaling law. Icarus 262, 79–92. doi:10.1016/j.icarus.2015.08.035.

Wright, E., Quillen, A.C., South, J., Nelson, R.C., Sánchez, P., Siu, J., Askari, H., Nakajima, M., Schwartz, S.R., 2020. Ricochets on asteroids: Experimental study of low velocity grazing impacts into granular media. Icarus 351, 113963. doi:10.1016/j.icarus.2020.113963.

Wünnemann, K., Zhu, M.H., Stöffler, D., 2016. Impacts into quartz sand: Crater formation, shock metamorphism, and ejecta distribution in laboratory experiments and numerical models. Meteoritics & Planetary Science 51, 1762–1794. doi:10.1111/maps.12710.